Flow instability and transient flow patterns inside intercrossed silicon microchannel array in a micro-timescale

J.L. Xu [a,*], W. Zhang [a,b], Q.W. Wang [c], Q.C. Su [a,b]

[a] *Micro Energy System Laboratory, Guangzhou Institute of Energy Conversion, Chinese Academy of Sciences, Nengyuan Road, Wushan, Guangzhou 510640, People's Republic of China*
[b] *The Graduate School of Chinese Academy of Sciences, Beijing 100039, People's Republic of China*
[c] *State Key Laboratory of Multiphase Flow, Xian Jiaotong University, Xian 710049, People's Republic of China*

Abstract

The objective of this study is to visualize the transient flow patterns and heat transfer behaviors at low mass fluxes and high heat fluxes. The silicon chip consists of the intercrossed microchannel array with 10 triangular microchannels with the hydraulic diameter of 155.4 μm, and five transverse trapezoid microchannels, separating the triangular microchannels into six independent zones. The chip is horizontally positioned. Liquid acetone is used as the working fluid. Tests were performed in the range of mass flux 40–80 kg/m² s and heat flux 107–216 kW/m².

It is found that all the microchannels repeat the flow patterns in the timescale of milliseconds, with three substages: liquid refilling stage, transient stratified flow stage and partial/fully dry-out stage.

Stratified flow is the dominant flow due to the low liquid Froude numbers. The axial liquid film thickness for each separated microchannel zone is increased along the flow direction, caused by the large momentum force due to evaporation on the interface of the vapor and the settled liquid film, and the high vapor shear stress applied on the vapor/liquid interface. The non-uniform axial liquid film distributions cause the earlier dry-out of the triangular microchannel upstream. However, dry-out always takes place earlier in the downstream zone than that in the upstream zone. The vapor slug near the triangular microchannel exit may be entrained in the long liquid plug during the liquid refilling stage. Besides, the steep jumped liquid film thickness may take place near the channel exit for the stratified flow. Both indicate the strong geometry effects.

Due to the compact size and high thermal conductivity of the silicon chip, the chip surface temperature variations versus time are identified by the infrared radiator image system, especially in the ending area of the thin film heater.
© 2006 Elsevier Ltd. All rights reserved.

Keywords: Microchannel; Flow patterns; Flow instability; Micro-timescale; Stratified flow; Liquid film

---

* Corresponding author. Tel./fax: +86 20 87057656.
   E-mail address: xujl@ms.giec.ac.cn (J.L. Xu).

1. Introduction

An important topic in the two-phase flow and heat transfer field is the flow instabilities, which have been studied widely in the past several decades in macroscale. They can take place in nuclear reactors, boilers, heat exchangers, etc, leading to the mechanical vibration, the disturbance of the electronic control device, the local overheating of the heat transfer surface and the high thermal stress of the solid walls (Ding et al., 1995).

The two-phase flow instabilities consist of the static and dynamic flow ones. The static flow instabilities can be caused by the flow rate excursion, the transition from one flow pattern to another one, and the transition of the heat transfer mechanisms. The commonly encountered dynamic flow instabilities are the pressure drop type oscillations, the density wave oscillations, and the thermal oscillations. The thermal oscillations are not independent ones, but sometimes occur accompanying with other type of flow instabilities. Almost all of the dynamic flow instabilities take place with large oscillation amplitudes and long cycle periods. The cycle periods are in the order of seconds and even minutes. These flow instabilities are well studied in macroscale, due to their wide applications in industries.

There are increasing numbers of articles dealing with the single/two-phase flow and heat transfer in micro-channels. This is due to the high demand for the understanding and application of the micro devices or systems for high heat flux electronic cooling, bio-MEMS chip, micro thrusters, etc. However, little studies were performed for the two-phase flow instabilities in microchannels. Wu and Cheng (2003a) reported the experimental studies with water as the working fluid flowing in horizontal silicon microchannels. Various modes of boiling instabilities occur after the boiling incipience. An unsteady liquid/two-phase/vapor alternative flow (LTVAF) takes place in the microchannels. Wu and Cheng (2003b) used two sets of parallel micro-channels with the hydraulic diameters of 155.8 μm and 82.8 μm. It is found that the fluid pressures, wall temperatures and flow rates are oscillating with large amplitudes and long periods. With the aid of a micro-scope and a high speed camera, the flow patterns were observed such as bubbly flow, slug flow, churn flow and other peculiar flow patterns. They stated that such kind of flow instabilities occurring in microchannels can be self-sustained if the pressure drops and the mass flow rates have phase differences. Wu and Cheng (2004) reported the further studies on the two-phase flow instabilities with the hydraulic diameter of 186 μm and the length of 30.0 mm. Three types of flow instabilities appear: the liquid/two-phase alternative flow at low heat fluxes and high mass fluxes, the continuous two-phase flow at medium heat fluxes and mass fluxes, the liquid/two-phase/vapor alternative flow at high heat fluxes and low mass fluxes. Again some flow patterns were observed.

Peles et al. (2001) concerns the forced convective liquid flow in heated microchannels, dividing the whole flow length into the liquid part and the vapor part. A number of dimensionless parameters, such as the Peclet number (Pe), Jacob number (Ja) and dimensionless heat fluxes, are defined. Both of the numerical and experimental findings show that boiling two-phase flow in capillary channels is unstable for the outlet mean vapor mass qualities less than unity. In a recent study by Hetsroni et al. (2005), it is found that long vapor bubbles occurring in microchannels at low liquid Reynolds number, which is not similar to the classical annular flow. This phenomenon is considered as the explosive boiling with periodic wetting and dry-out. The pressure drops are found to be oscillating which is enhanced with increasing the vapor mass qualities.

Xu et al. (2004) conducted an experiment in a single capillary stainless tube with the inside diameter of 500 μm. Two types of flow instabilities were identified. The first type is the long period/large amplitude liquid/two-phase alternative flow, occurring at the inlet liquid temperature of nearly saturated condition. It regards the feedback control of the mass flow rate in the capillary tube and the entrance liquid temperature of the microtube, incorporating the system geometry, dimensions and the microchannel itself. The second type of unsteady flow occurs when the liquid temperature in the water tank varying from room to 80 °C, and it is named as the long period/small amplitude periodic subcooled boiling. Xu et al. (2005a) conducted the static and dynamic flow instability of a parallel copper microchannel heat sink at high heat fluxes using water as the working fluid. The onset of flow instability (OFI) occurs at the channel outlet temperature of 93–96 °C, which is several degrees lower than the saturated temperature of 100 °C corresponding to the exit pressure. If the mass flow rate is less than that of OFI, three types of flow instabilities appear: the large amplitude/long period oscillation, the small amplitude/short period oscillation. The thermal oscillations are observed to be accompanying the above two oscillations.

Recently, Xu et al. (2005b) performed the microscale boiling heat transfer using acetone as the working fluid in 10 parallel straight silicon microchannels with each hydraulic diameter of 155.4 μm. The transient flow patterns were carefully observed using a microscope bonded with a high speed camera. The chip temperatures were measured using an infrared radiator image system. The transient flow patterns are repeated in a timescale of milliseconds. A full cycle can be subdivided into three substages: liquid refilling stage, bubble nucleation, growth, and coalescence stage and transient annular flow stage. Four flow patterns are observed. Paired or triplet bubbles nucleate, grow up and coalescence simultaneously in, or very close to the channel corners at the same cross-section. Bubble explosive takes place once the paired or triplet bubbles coalescence in the same cross-section of the microchannel and pushes the fluid out of the microchannels both upstream and downstream. Then a fresh liquid reenters the microchannels. Xu et al. (2005c) extends the above work and provides a link between the transient flow patterns and the measured boiling heat transfer behaviors. Five heat transfer mechanisms could be deduced from the transient flow patterns based on the four observed flow patterns. The boiling numbers are found to characterize the microscale boiling heat transfer coefficients, which can display three different regions by dividing the boiling numbers into three subranges. The transient flow pattern based microscale boiling heat transfer mechanisms are well consistent with the measured heat transfer coefficients with the effects of heat fluxes, mass fluxes and vapor mass qualities. In summary, two-phase flow instabilities in microscale are far to reach the general conclusions at this stage.

When the hydraulic diameter is less than the criterion of $[\sigma/g(\rho_G - \rho_L)]^{0.5}$, where σ is the surface tension force, g is the gravity acceleration, ρ_L and ρ_G are the liquid and gas densities respectively, the "microscale effects" become evident. The hydraulic diameter of $D = 155.4$ μm was smaller than the above criterion.

Kandlikar (2004) summarized most of the non-dimensional parameters relevant to two-phase flow in microchannels. For a specific silicon chip operating at high heat fluxes, different operation range yields the different magnitudes of the non-dimensional parameters, leading to the different flow pattern and heat transfer response (Xu et al., 2005c). Besides, the studies by Lee et al. (2003) show that the microchannel size and shape also have effects on the boiling heat transfer behavior.

It is noted that almost all of the microscale boiling heat transfer experiments were performed using single or parallel straight microchannels. However, due to the different applications, the micro structures in micro devices or systems sometimes are quite complicated, such as the micro-pin-fin structure, the curved microchannels, the intercrossed microchannel arrays etc. There are two main objectives for the present study: (1) to obtain the flow patterns and heat transfer behaviors in the intercrossed microchannel array. (2) to investigate the flow patterns and heat transfer behaviors at high heat fluxes and low mass fluxes. Such parameter combinations are the worse runs that a micro-evaporator may encounter, but the critical heat flux is never encountered. The silicon chip, which is horizontally positioned, consists of 10 triangular microchannels along the longitudinal direction, and five transverse trapezoid microchannels, separating the triangular microchannels into six independent zones. Each transverse trapezoid microchannel acts as the outlet of the previous ending zone and the inlet of the next coming zone.

2. The intercrossed silicon microchannels and the experimental setup

2.1. The intercrossed microchannel array and its fabrication

The micro evaporator with the intercrossed microchannel array is made of silicon with the thickness of 525 μm, bonded with the pyrex glass plate with the thickness of 410 μm (see Fig. 1). The whole silicon chip has the total length of 30.0 mm and the width of 7.00 mm. Each triangular microchannel has the width of 300 μm and the depth of 212 μm, forming the hydraulic diameter of 155.4 μm. The 10 triangular microchannels cover the total width of 4.35 mm. The whole length of the triangular microchannels in longitudinal direction is 21.45 mm. Five transverse trapezoid microchannels are uniformly arranged along the flow direction, forming six independent zones. The centerline distance between each transverse microchannel is 3.694 mm. The transverse trapezoid microchannels have the top width of 1.015 mm and the same depth of 212 μm as the triangular microchannels, which are acted as the outlet of the previous parallel triangular microchannel and the inlet of the next parallel triangular microchannels. The cross-sectional view (A–A) and the longitudinal directional view (B–B) are shown in Fig. 1. The thin Pt film was deposited on the back surface of the silicon
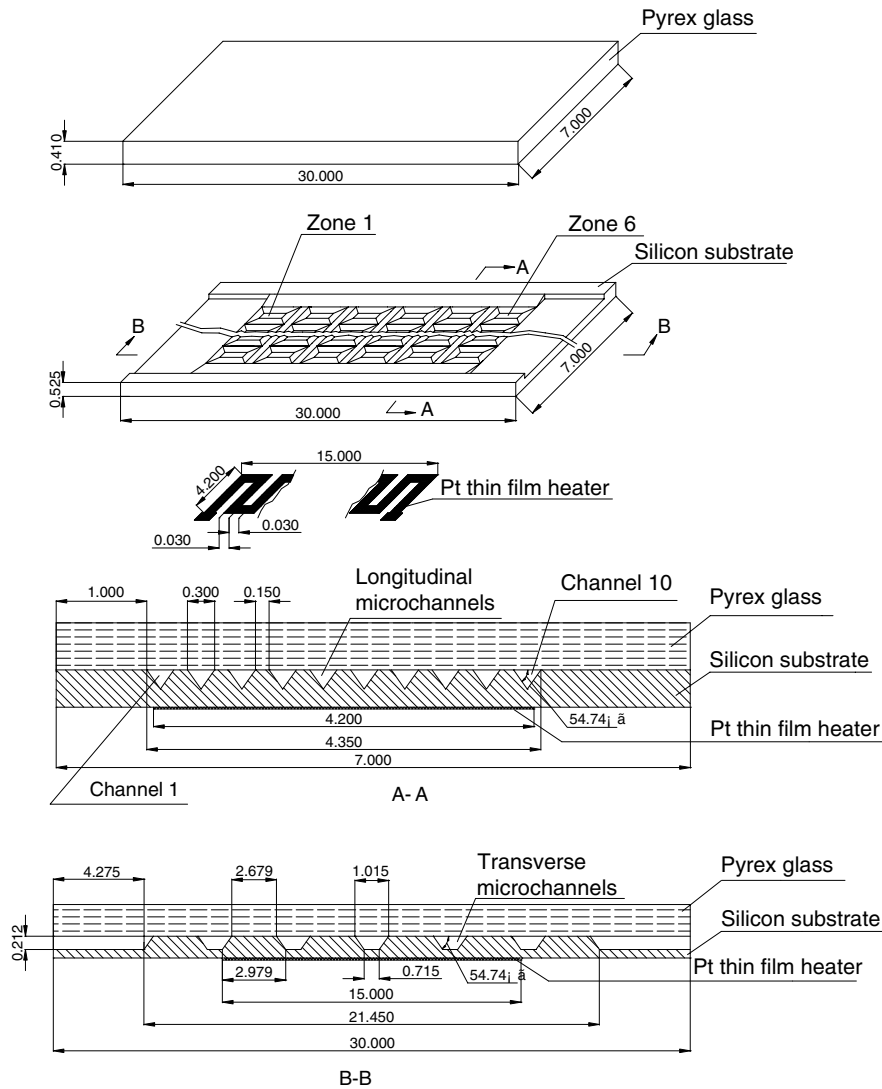
Fig. 1. The intercrossed microchannel array used in the present study (all dimensions are in mm).

chip, covering the film area of 21.45×4.20 mm^2. However, the effective heating area is 15.0×4.2 mm^2, central-ized located on the back silicon chip surface.

The present intercrossed silicon microchannel array is designed based on the idea that each microchannel length for an independent zone is shorter so that thermal developing flow is ensured in each independent zone, which enhances heat transfer for single-phase liquid flow (Xu et al., 2005d). The present paper is to examine the two-phase flow and heat transfer behaviors in such intercrossed microchannel arrays.

The silicon chip is fabricated using <100> double polished wafers with the size of 4 inch. The standard MEMS fabrication technique is applied: double side thermal oxidation layers and nitride layers deposited on the wafer to 3000 Å and 1500 Å, respectively. A standard photoresist layer spun on the wafer and warmed as conventional and the lithographic processing technique applied, Reactive Ion Etching (RIE) of the nitride layer and the oxide layer by 1500 Å and 3000 Å respectively, top side photoresist removal, wet etching of the microchannel by the depth of 212 μm using KOH, backside RIE of the nitride and oxide layers, backside photoresist removal, top side silicon nitride and oxide removal by RIE, silicon chip bonded with the pyrex glass plate, backside photoresist and lithographic procedure applied, backside titanium layer and Pt film deposed to both of 1000 Å.

2.2. The experimental setup and the measurement systems

The experimental setup is shown in Fig. 2a. A forced convective loop was built with three subsystems: the liquid supply subsystem, the silicon chip test section and the optical measurement subsystem, and the liquid collection subsystem. The liquid supply subsystem includes the nitrogen gas bottle, the high precision pressure regulator, the liquid tank and the temperature control unit. Liquid acetone inside the tank, with the temperature control uncertainty of 0.5 °C by the PID temperature control unit, is pressurized by the high pressure nitrogen gas and flows successively through a 2 micron filter and the silicon chip. The two-phase mixture out of the silicon chip is condensed by the condenser and collected by the liquid beaker, which was put on the top surface of the high precision electronic balance.

The inlet and outlet fluid temperatures (T_{in} and T_{out}) were measured by the high precision K type jacket thermocouples with the accuracy of 0.3 °C. The condensed liquid was measured by the electronic balance with
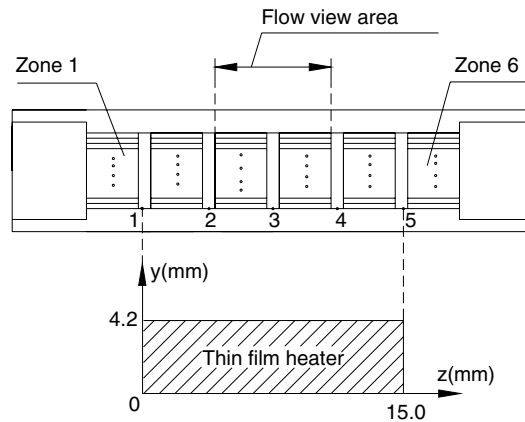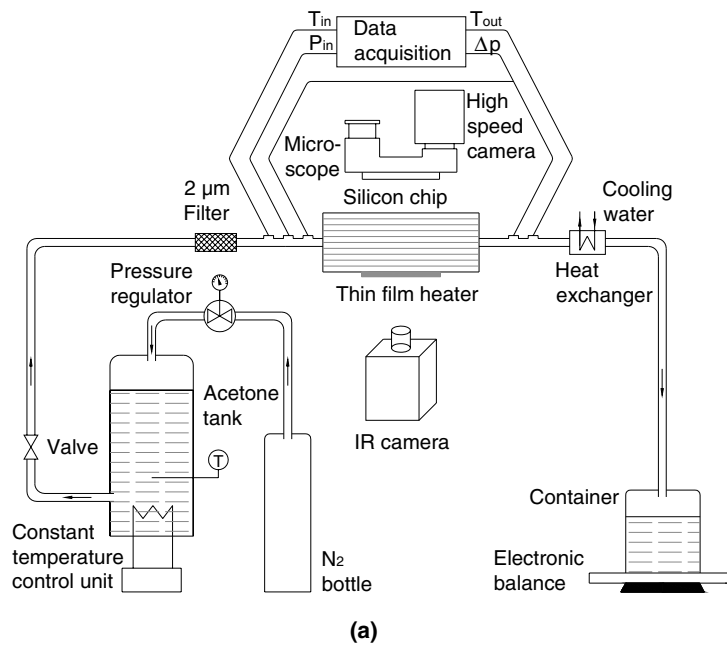

Fig. 2. The experimental setup (a) and the coordinate attached on the focused thin film heater (b).

the accuracy of 0.02 g. The mass flow rate was decided by the increased liquid weight over a given period of time. The inlet pressure (p_{in}) was measured by a Setra pressure transducer (model 206) with the accuracy of 1% after calibration with a known standard. The pressure drops across the silicon chip (Δp) are measured by a Senex differential pressure transducer with the uncertainty of 0.1%. The response time of the pressure, the differential pressure transducer and the thermocouples are 0.1 s, 0.01 s and 0.2 s respectively.

The transient flow patterns were observed by our joined optical system. The microscope is a Leica M stereo microscope (Germany). When the microscope is running, a powerful cold light source is turned on to form the clear image. However, the microscope is bonded with our high speed camera system (Redlake, Inc, USA) with a one inch C-type port. The high speed camera system has the maximum recording rate of 20,000 frames/s with the resolution of 1504×1128 pixels. Much higher recording rate needs very powerful light source. In the present study, a high speed recording rate of 1000 or 2000 frames/s was used. The flow visualization view area was focused on the zone 3 and 4 (the two center regions of the silicon chip, see Fig. 2b). It is noted that the flow view area should be balanced between the longitudinal and transverse directions. The flow pattern images are not clear if all the six independent zones are in the view area. It is the top view through the transparent cover that captures the dynamic flow patterns inside the microchannel array.

A thin black lacquer was uniformly painted on the back surface of the silicon chip. The temperature field of the backside silicon chip surface was measured by a high-resolution high-accuracy infrared radiator image system (FLIR ThermaCAM SC3000 IR). The thermal sensitivity at the room temperature is 0.02 °C and the typical resolution of 320×240 pixels over the whole heating area. These parameters ensure the precise determination of the maximum temperature and the maximum temperature gradients over the heated surface, which cannot be fulfilled using the conventional method of thermocouples. The view area of the IR image system is focused on the effective heating area of 15.0×4.2 mm^2. It is noted that the surface temperature measurements by the IR image is also reported by Hetsroni et al. (2003, 2005).

The relative positions of the flow view area, the whole intercrossed microchannel array, the whole silicon chip and the effective heating area that is exposed in the IR camera view, are shown in Fig. 2b. The optical flow field view area is 7.39×4.35 mm^2 for the flow pattern observations, which covers the whole microchannel width, but covers 49% of the total effective heating length (7.39 mm relative to 15.0 mm). The flow visualization area is for zone 3 and 4 of the microchannel array, while the focused area of the IR image system corresponds to zones 2, 3, 4 and 5 of the microchannel array. The y–z coordinates are attached on the effective heating film, with the z-coordinate for the axial flow direction and y-coordinate for the width direction. An ac power supply system drives the thin Pt heating film. The heating power is obtained from a precision power-meter. The heat generated by the thin film heater is transferred to the fluid inside the microchannel array of the silicon chip.

In the present study, we stabilize the pressure drop across the silicon chip around 30 kPa. Liquid acetone is pressurized into the chip and the single-phase liquid flow inside the loop is established. Then the heat flux is applied gradually, until the two-phase flow is established. For each heat flux run, we stay the system for at least half hour to wait for a self-sustained "stable" state is reached. Then the two optical systems are running to collect the high speed images and the IR images. Meanwhile the data acquisition system collects the pressure, pressure drop and temperature signals. All the data files are collected by two independent computers for future analysis.

In the present paper we focus on the transient flow patterns in microchannel arrays with the millisecond timescale using the microscope and the high speed camera system. The optical system has the time resolution of 1 or 0.5 ms, depending on the recording rate used. The cycle periods of the transient flow identified in the present paper are in the range of 26–64 ms. Thus the optical system is fast enough to capture the transient flow. The transient flow is identified by the high speed camera system, not by the pressure and temperature sensors. Because the pressure and temperature sensors with the high recording rate up to 1000 Hz at least are not available, these sensors may not capture the transient flow in millisecond timescale.

The present experiments cover the following data ranges: inlet liquid temperatures from 28 to 33 °C, the heat fluxes from 107 to 216 kW/m^2. The corresponding mass fluxes are varied from 40 to 80 kg/m^2 s, and the exit vapor mass qualities are varied from 0.8251 to 1.3214.

It is noted that the vapor mass qualities are defined as $x = (h - h_{L})/h_{LG}$, where h, h_{L} and h_{LG} are the fluid enthalpy, saturated liquid enthalpy and latent heat of evaporation, respectively. Vapor mass qualities larger

than unity are for the superheated vapor state, that may be encountered for the low mass flux and high heat flux runs in the present paper.

2.3. Data reduction and uncertainty analysis

The pure liquid acetone (CH_3COCH_3, molecular weight of 58.08 and the purity > 99.5%) is used as the working fluid. Its physical properties can be found in Yaws (1999). It has the saturated temperature of 56.3 °C at the environment pressure. Even though the microchannel array used in the present paper is different from our previous studies (Xu et al., 2005b), the similar data reduction procedure was applied. All the parameters are defined in terms of the 10 triangular microchannels along the longitudinal direction without consideration of the transverse trapezoid channels. The liquid Reynolds number (Re), the average mass flux (G) and the effective heat flux (q) are defined as $Re = UD/v$, $G = m/(N_L A_C)$, and $q = \varphi VI/(2N_L b L_h)$ respectively, where U is the mean liquid velocity assuming the total two-phase mixture flowing as the liquid only, v is the liquid kinematic viscosity computed at the inlet liquid temperature, m is the mass flow rate determined by the electronic balance, N_L is the total number of the triangular microchannels, A_C is the cross-sectional area of the triangular microchannel, φ, V and I are the thermal efficiency, voltage and current that applied on the thin film heater, b and L_h are the side wall width of the triangular microchannel and the effective heating length. The vapor mass qualities are calculated based on the fluid enthalpy increment from the entrance. The five vapor mass qualities are calculated corresponding to the axial locations of 1, 2, 3, 4 and 5, as shown in Fig. 2b.

We compute the boiling heat transfer coefficients over the effective heating area of 15.0×4.2 mm^2 relevant to the flow direction (z-coordinate) and the width direction (y-direction). The whole effective heating area is divided into two areas, the single-phase liquid flow area and the two-phase flow area. The energy conservation equation gives the length of the single-phase liquid area as

$$L_{sp} = mC_{pL}L_h(T_{sat} - T_{in})/Q \tag{1}$$

where C_{pL} is the liquid specific heat, L_h is the effective heating length, T_{sat} and T_{in} are the saturated and inlet liquid temperatures respectively, Q is the effective heating power that is calculated from the measurement of the powermeter (V and I readings from the powermeter) timing the thermal efficiency φ, which will be discussed later.

The linear liquid temperature assumption along the flow direction is made in the liquid flow area. The liquid temperature ($T_L(z)$), the local vapor mass quality ($x(z)$) and the heat transfer coefficient ($h(z,y)$) are computed as

$$T_L(z) = T_{in} + (T_{sat} - T_{in})z/L_{sp} \tag{2}$$

$$x(z) = \frac{C_{pL}(T_{in} - T_{sat}) + zQ/mL_h}{h_{LG}} \tag{3}$$

$$h(z,y) = \frac{q}{T_w(z,y) - T_L(z)} \tag{4}$$

where T_w is the chip wall temperatures measured by the IR image system. $x(z)$ in Eq. (3) is negative in the liquid flow area and positive in the two-phase flow area. In Eq. (4) $T_L(z)$ is the liquid temperature computed using Eq. (2) in the liquid flow area and is replaced by the saturated temperature of T_{sat} in the two-phase flow area. Distinct with other studies, the local heat transfer coefficients are determined based on the local IR temperature measurements, while this cannot be fulfilled using the conventional methods such as thermocouples.

In addition to the above parameter definitions, there are some parameters that are useful for the analysis in the flow patterns and heat transfer behaviors for the present studies. The boiling numbers are defined as $Bo = q/Gh_{LG}$. The liquid Froude numbers are defined as $Fr_L = U^2/gD$. The present study concerns the low liquid Froude numbers and high boiling numbers. The boiling numbers cover the range of 3.57×10^{-3} to 6.28×10^{-3}, and the liquid Froude numbers cover the range of 1.87–7.31.

The direct measurement parameters have the following uncertainties: the microchannel upstream pressure of 1%, the pressure drop across the microchannels of 0.1%, the inlet/outlet fluid temperatures of 0.3 °C, and

the chip temperature measurements using the IR image system of 0.4 °C. The above deduced liquid Reynolds numbers and mass fluxes have the errors of 2.96% and 2.1% respectively, using the standard error analysis. It is quite difficult to decide the effective heating power due to relative larger surface to volume ratio of the silicon chip, which is influenced by a lot of parameters. The heat loss from the silicon chip to the environment includes the radiation and natural convection heat transfer from the heated wall surface to the environment. The heat loss also includes the heat conduction from the silicon chip to its upstream and downstream connection tubes. The calibration experiments for the thermal efficiency were performed before the boiling heat transfer experiments. The thermal efficiency is defined as the net heat received by the liquid acetone (determined by the mass flow rate and the liquid temperature difference across the silicon chip) over the total heating power. It is found that the thermal efficiency is strongly depended on the applied heating power. Always the higher the applied heating power is, the higher the thermal efficiency is. The mean averaged thermal efficiency φ is 0.84. The largest and lowest values are 0.90 and 0.77 respectively.

3. Results and discussion

3.1. Air–water flow calibration of the optical system

Before performing the microscale boiling heat transfer experiments, the optical system is calibrated to identify the liquid and gas phases using air–water mixture as the working media. The microchannels are occupied by the air initially. Then the liquid water was pumped into the silicon chip. Fig. 3 shows the gas–water coexisting inside a single triangular microchannel. The white image represents the liquid plug while the black image indicates the gas slug. This is always true for all of our tests in the present paper. The interface between the liquid plug and the gas slug is flat. The flow direction is from left to right. The white straight line shown in Fig. 3 is the liquid film that is drawn in the microchannel corners due to the surface tension effect.

3.2. Transient flow patterns in a micro-timescale

As noted in the introduction section, most of the two-phase flow instabilities occur accompanying the oscillations of pressures, fluid and wall temperatures and mass flow rates, such as the pressure drop type oscillations, the density wave oscillations in macroscale. However, the present paper identifies that these signals are stable, as shown in Fig. 4 for a typical run. This is because the response times of the pressure and temperature sensors are longer than the millisecond timescale of the transient flow, which is identified by the optical system. The transient flow patterns are shown in Fig. 5 for the same run as in Fig. 4. The flow pattern images for the whole 10 microchannels are selected from a successive of images using the recording rate of 1000 frames per second. It is seen that the whole microchannel array of the silicon chip repeat the flow patterns periodically with the cycle period of 53 ms. Such transient flow patterns are similar to all of the other runs in the present paper. Generally three substages exist: the liquid refilling stage, the transient stratified flow stage, and the partial or fully dry-out stage, which are described as follows.

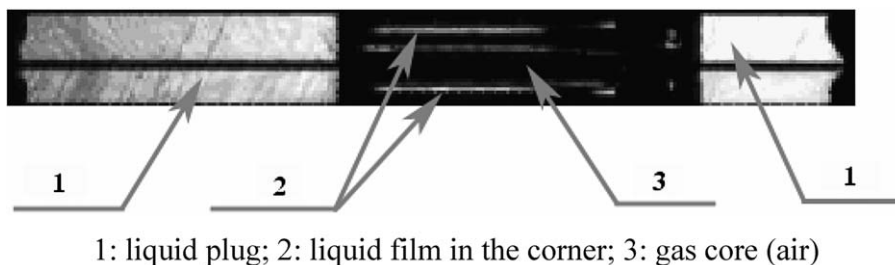1: liquid plug; 2: liquid film in the corner; 3: gas core (air)

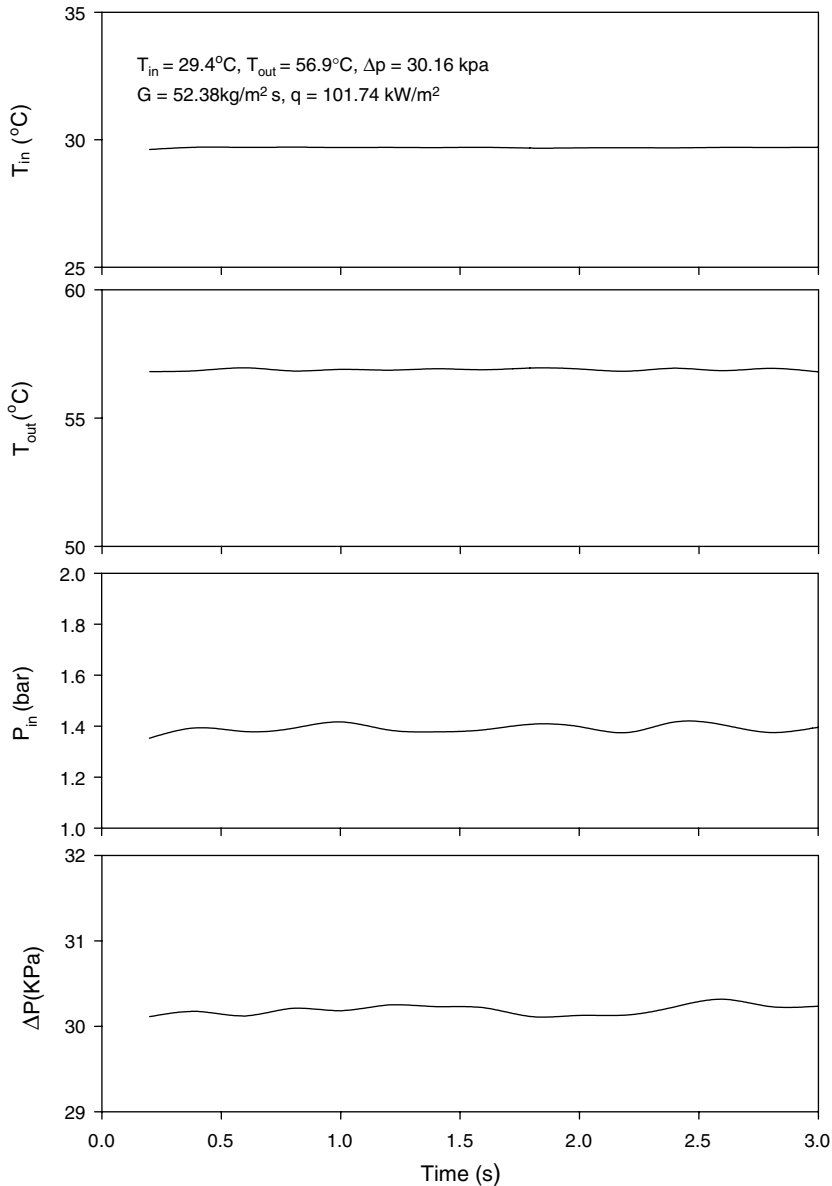Fig. 3. Air–water calibration result in a single triangular microchannel.

Fig. 4. Quasi-stable fluid pressure, pressure drop and temperature output versus time.

3.2.1. Liquid refilling stage (0 < t < 2 ms)

Partial dry-out (microchannel upstream dry-out, represented by the black spot) in zone 3 and nearly fully dry-out (full black area) in zone 4 take place at $t = 0$ in Fig. 5. This image is actually the end of the previous cycle. Suddenly all the microchannels in zone 3 are refilled by the liquid at $t = 1$ and 2 ms but the microchannels in zone 4 are still in the dry-out state, indicating the beginning of a new cycle. In such a short period, the microchannels display the single-phase liquid convective heat transfer in zone 3 but the single-phase vapor heat transfer in zone 4. The contributions of these two heat transfer mechanisms in the two zones should be small because this stage covers a small percentage of a full cycle.

3.2.2. Transient stratified flow stage (3 ⩽ t < 29 ms)

Liquids in the microchannels for zone 3 soon evolve the stratified flow following the time of $t > 3$ ms, indicated by the two parallel white lines for each triangular microchannel. The liquids are settled down to the bot-

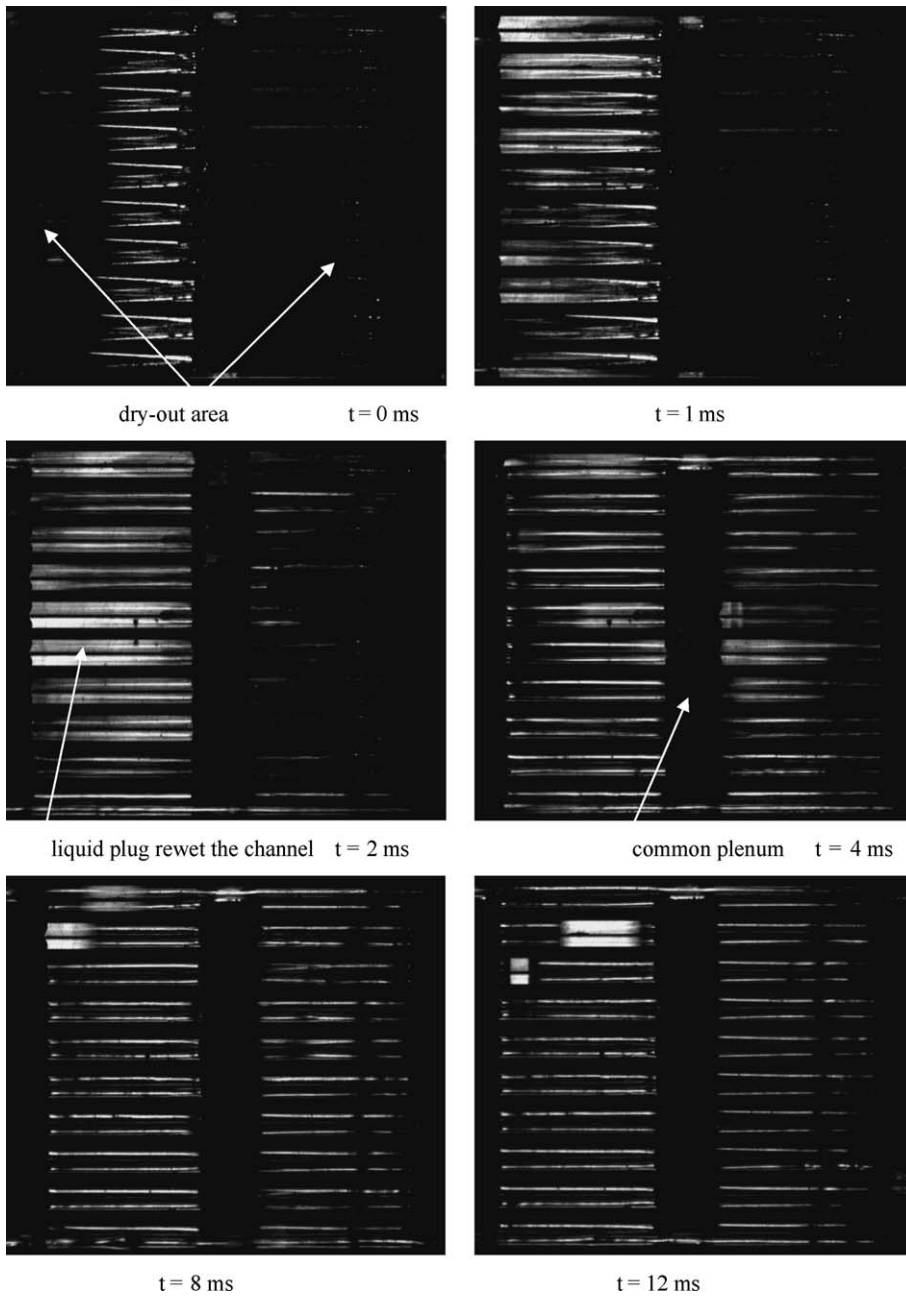Fig. 5. A set of images showing the cycle behavior ($T_{in} = 29.4$°C, $T_{out} = 56.9$ °C, $\Delta p = 30.16$ kPa, $G = 52.38$ kg/m^2 s, $q = 101.74$ kW/m^2).

tom of the microchannels in zone 3, which is analyzed by scaling the size of the relative position of the two side microchannel corners and the two white lines (will be described later). The microchannels for zone 4 are also rewetted by the liquids coming from its inlet trapezoid common plenum in the early of this substage. However such liquids are also settled down to the bottom of the microchannels, similar to zone 3. Checking a successive of images clearly shows that the dual white lines for each microchannel for both zones become dark and dark versus time, indicating that the liquid films become thin and thin with time evolving. In this substage, some peculiar flow patterns are observed and were not reported previously. These commonly encountered flow structures in the present study are: the short liquid plug oscillating in some microchannels, the vapor slug near
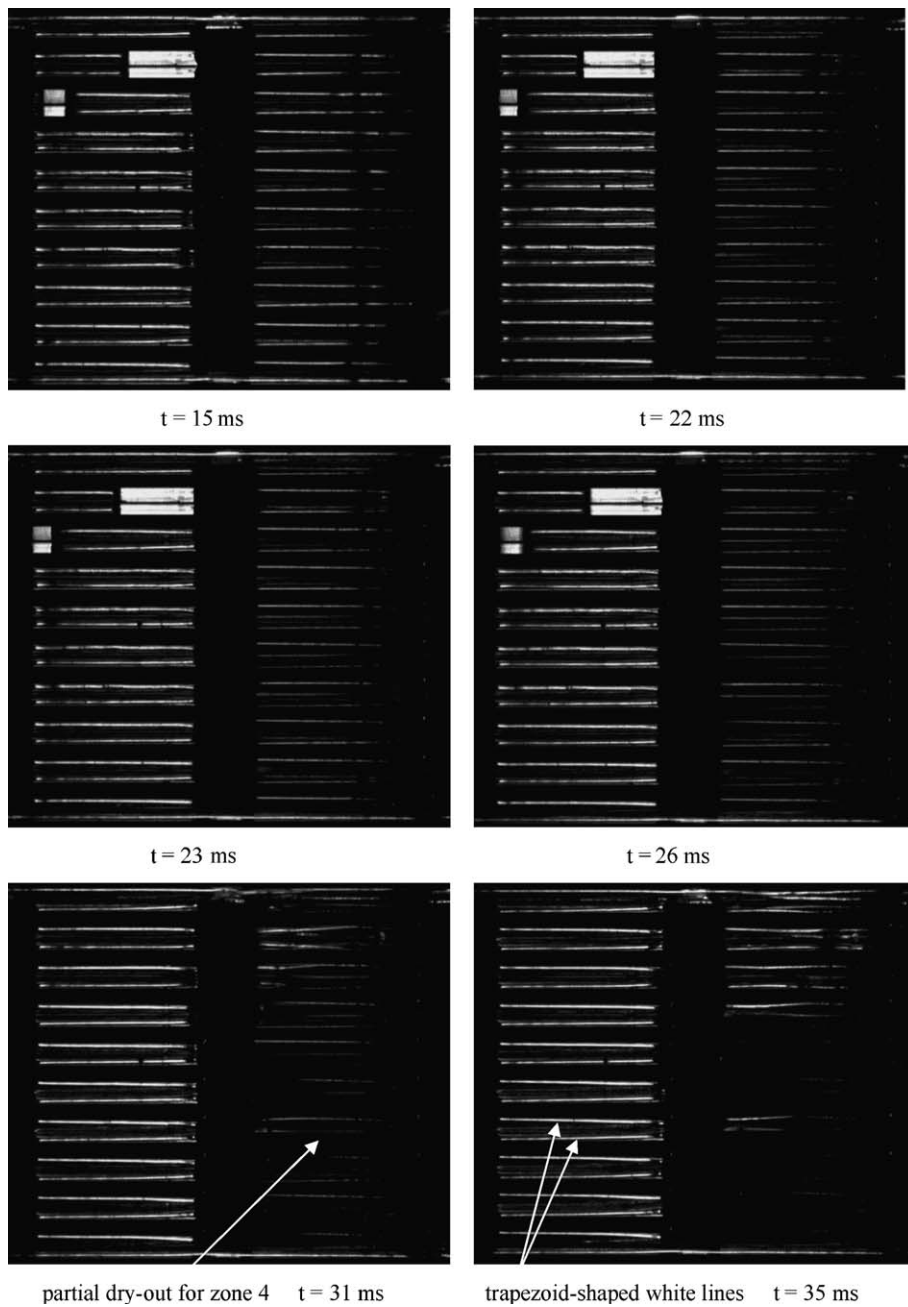
t = 15 ms   t = 22 ms

t = 23 ms   t = 26 ms

partial dry-out for zone 4   t = 31 ms   trapezoid-shaped white lines   t = 35 ms

Fig. 5 (*continued*)

the channel exit entrained in the long liquid plug, the stratified flow with uniform and non-uniform liquid films along the flow direction, and the stratified flow with the steep jumped film thickness near the channel exit. These phenomena will be described later in detail. Heat transfer in this stage is mainly characterized by the liquid film evaporation mechanism.

3.2.3. Transient stratified flow pattern and partial/fully dry-out stage $(30 \leqslant t < 53 \text{ ms})$

It is found that in a full cycle the dry-out state takes place earlier in the downstream zone than that in the upstream one. The dynamic images show that the images are always darker in zone 4 than those in zone 3. For

t = 37 ms

t = 39 ms

t = 42 ms

t = 47 ms

t = 49 ms

channel upstream dry-out   t = 53 ms
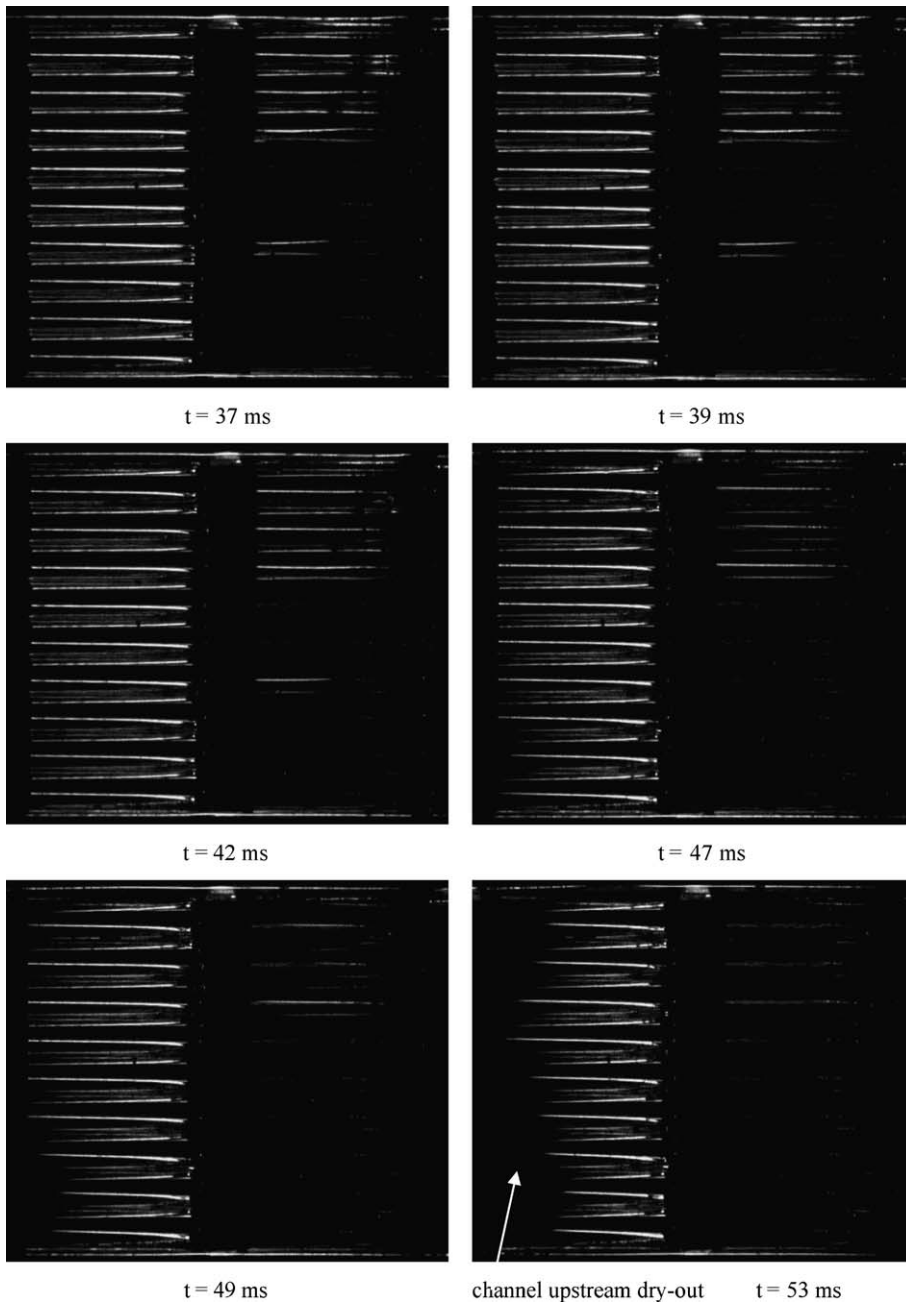
Fig. 5 (*continued*)

instance, the dry-out spot occurs following the time of 31 ms in zone 4, while the dual-white-lines can still be seen for each microchannel of zone 3, until $t = 47$ ms. This is easy to be understood because the mean vapor mass qualities are always higher in zone 4 than those in zone 3.

However, for each separated zone, the dry-out state occurs earlier in the upstream area than that in the downstream area, corresponding to the inverse axial liquid film distribution. In other words, the liquid film thickness is increased along the flow direction. The "early microchannel upstream dry-out" behavior can be identified following the time of 49 ms. In the end of the selective cycle, the microchannel upstream area

is dry-out but the microchannel exit area close to the common plenum is still covered by the axial trapezoid liquid films for zone 3. The image at $t = 53$ ms repeats the status at $t = 0$ of this cycle.

In order to further identify the cycle behavior in the timescale of milliseconds, we plot the cycle periods versus a successive of cycle numbers in Fig. 6 for the same run of Figs. 4 and 5. The cycle period for this run is from 50 to 58 ms, indeed display the perfect cycle behavior. In the present data range, the cycle period is mainly depended on the applied heat flux, as shown in Fig. 7. The higher the heat flux is, the shorter the cycle period is, indicating that the dynamic process becomes faster with increasing the heat flux. The cycle periods in the timescale of milliseconds identified in the present paper are at least one or two orders shorter than those of the commonly encountered two-phase flow instabilities such as pressure drop type, density wave type two-phase flow instabilities in macroscale. The response of the flow patterns are so fast that the electronic transducers, such as the fluid pressures and temperatures cannot trace such fast process, leading to the stable signal output versus time (see Fig. 4).

3.3. Comparison of the flow instabilities between the present and other studies

The silicon chip used in our previous studies (Xu et al., 2005b) is the same as the present one, except that there are no any transverse trapezoid microchannels. Both silicon chips display the transient flow patterns in
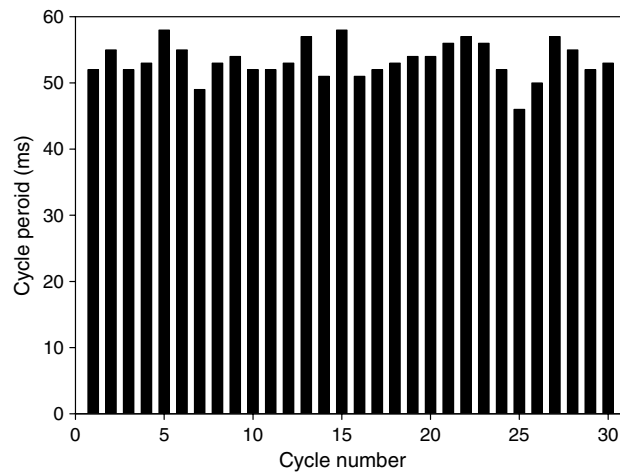

Fig. 6. Cycle period for different successive cycles ($T_{in} = 29.4$ °C, $T_{out} = 56.9$ °C, $\Delta p = 30.16$ kPa, $G = 52.38$ kg/m^2 s, $q = 101.74$ kW/m^2).
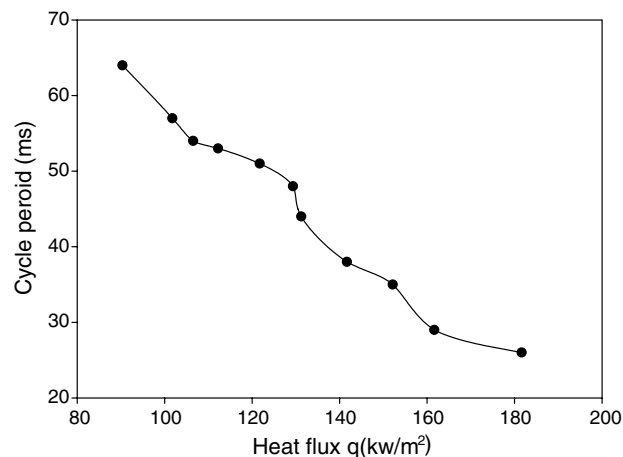

Fig. 7. Decreased cycle periods with increasing the heat fluxes.

the timescale of milliseconds, with the stable fluid pressures and temperatures versus time. The cycle periods are in the same order for both. However, the flow patterns are quite different, indicating the strong chip geometry effect. For the normal straight triangular microchannels (Xu et al., 2005b), group bubbles are always observed to be nucleated in or very close to the channel corners. Following then, bubbles are growing up quickly and evolve very quick coalescence in the same cross-section of the triangular microchannel in a couple of milliseconds. Once upon their coalescence, the superheated liquid releases its energy through the vapor/liquid interface, inducing the bubble explosive, pushing the fluid out of the microchannels both upstream and downstream in less than 1 ms. While the bubble nucleations are fully suppressed but the liquid film evaporation domains for the present intercrossed microchannel array.

As described in the introduction section, boiling flow instabilities were also observed by Wu and Cheng (2003a,b, 2004), in which the fluid pressures and temperatures are oscillating with large amplitude/long periods. The maximum cycle periods can be up to in the order of 100 s. Similarly, the recent studies by Hetsroni et al. (2005) also reports that "occurrence of single-phase liquid flow and two-phase liquid–vapor flow, which appear alternatively with time in the microchannel, leads to the pressure drop oscillations". Based on the authors' opinion, two-phase flow instabilities with large amplitude/long period oscillations of the pressures and fluid temperatures are not only related to the boiling heat transfer inside the chip, but also relevant to the whole forced convective loop such as the connection tubes and upstream compressible volume of the silicon chip. This behavior is similar to the pressure drop type oscillation in macroscale. However, there are no general definition and classification of the two-phase flow instabilities with large amplitudes and long cycle periods in microscale at the moment. The two-phase flow instabilities with transient flow patterns but with stable fluid pressures and temperatures reflect the flow pattern transitions inside the silicon chip but the other components of the forced convective loop do not have effects on the flow and heat transfer. Thus this type of flow instability may be named as the "flow pattern type two-phase flow instability" in microscale.
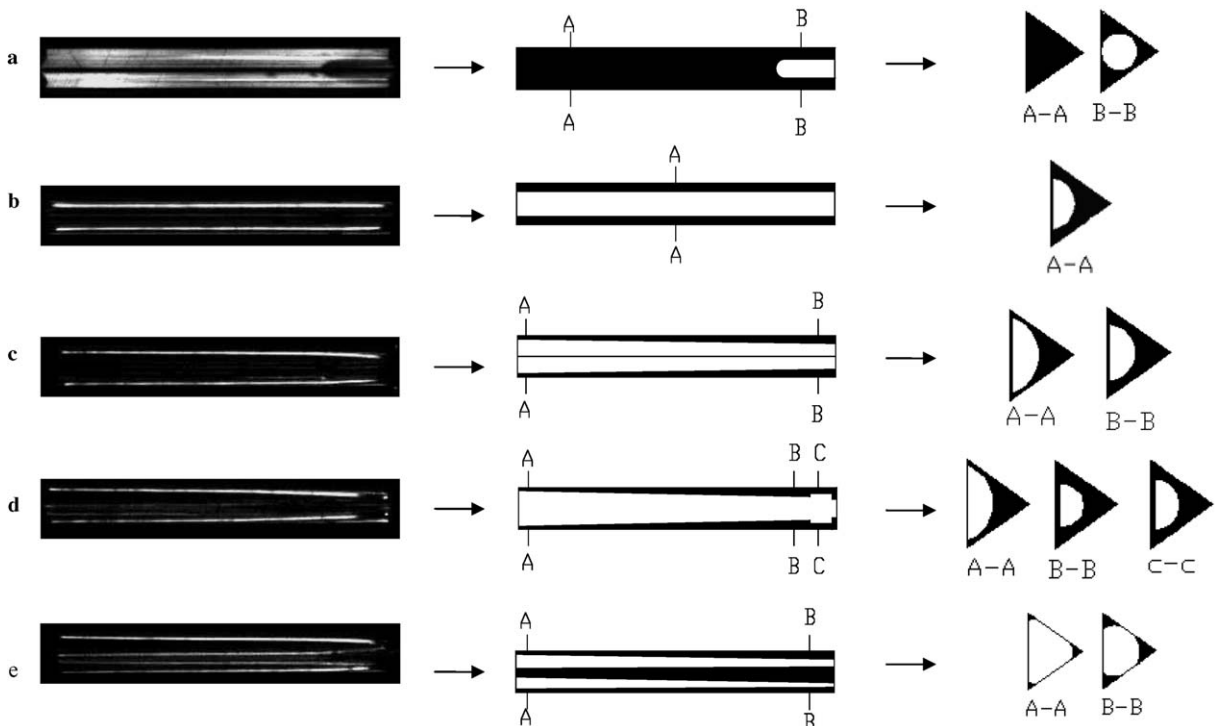

Fig. 8. Five flow patterns identified in the present paper.

3.4. Peculiar flow patterns

Fig. 5 shows the whole images of the 10 triangular microchannels for successive two zones (zone 3 and 4). We use the commercial software of PHOTOSHOP 6 to carefully check a set of images channel by channel and frame by frame for further study of the flow pattern details in single microchannel. For such analysis the relative positions between the channel corners and the white lines (indicating the interface between the liquid film and the vapor phase) is scaled in size. As noted early, it is the top view to observe the transient flow patterns and always the white image represents the liquid phase while the black image represents the vapor phase. In the present data ranges the stratified flow pattern is the dominant one characterizing the forced convective boiling heat transfer. However, five flow patterns can be identified, which are summarized in Fig. 8. These flow patterns are:

- Flow pattern A: the vapor slug near the channel exit entrained in the liquid plug;
- Flow pattern B: the stratified flow with liquids settled down to the bottom of the microchannels;
- Flow pattern C: the stratified flow with axial trapezoid-shaped liquid film distribution;
- Flow pattern D: similar to flow pattern C but the steep jumped liquid film near the channel exit;
- Flow pattern E: liquid films are accumulated only in the channel corners (partial dry-out state).

3.4.1. Flow pattern A

As shown in Fig. 8a, the whole selected microchannel for a separate zone is covered by the liquid phase with a standard vapor slug entrained in the body of the liquid plug close to the channel exit plenum. The dynamic formation of such flow pattern is illustrated in Fig. 9. It is noted that in the end of the previous cycle, the whole
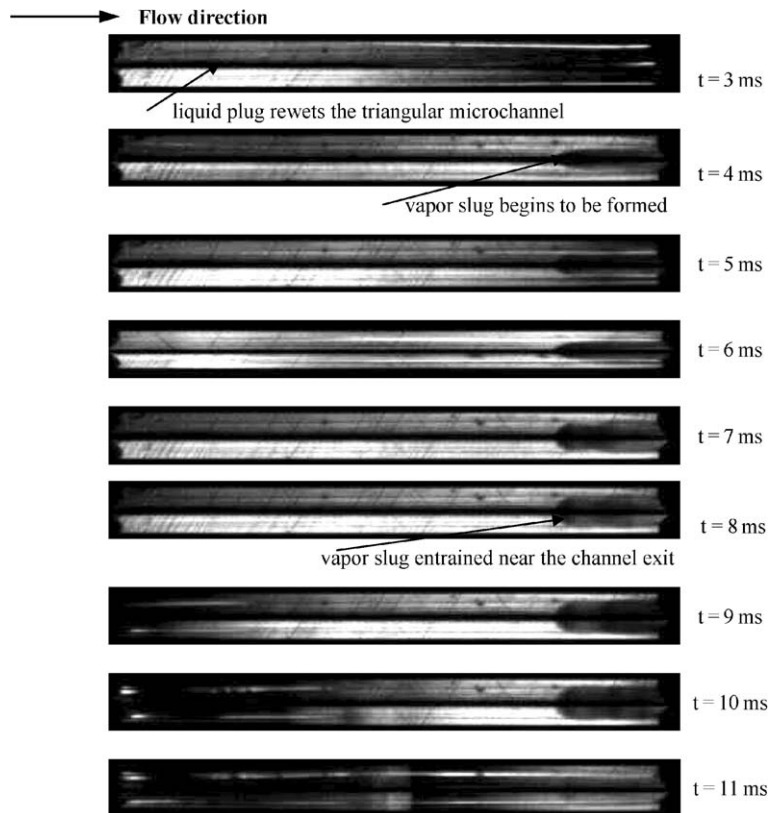

Fig. 9. Successive images showing the vapor slug entrained near the triangular microchannel exit (flow pattern A, $T_{in} = 28.1$ °C, $T_{out} = 58.4$ °C, $\Delta p = 30.77$ kPa, $G = 46.8$ kg/m^2 s, $q = 90.33$ kW/m^2, microchannel 9 in zone 3).

microchannel is full of vapor. Liquid plug from its inlet plenum begins to flush the triangular microchannel at $t = 3$ ms. When such front of the liquid plug nearly reaches the channel exit plenum, the outlet vapor slug begins to be formed at $t = 4$ ms. During the formation of the vapor slug, because the triangular microchannel is immersed by the liquid while the channel exit plenum is covered by the vapor, a positive pressure gradient along the streamwise direction near the channel exit plenum can be established, i.e., $dp/dz > 0$. The vapor slug can be lasted for several milliseconds ($4 < t < 10$ ms in Fig. 9) and disappeared accompanying the disappearance of the liquid plug in the triangular microchannel, at $t = 11$ ms (see Fig. 9). Flow pattern A generally takes place in the liquid refilling stage.

It is also observed that during the liquid refilling stage, occasionally a short liquid plug (see Fig. 10), instead of a long liquid plug as shown in Fig. 9, rewets the straight triangular microchannel. The short liquid plug generally has the flat interface with the vapor phases, separating the whole microchannel for a separate zone into three parts, with its both upstream and downstream of vapor phases. As shown in Fig. 10, the flow
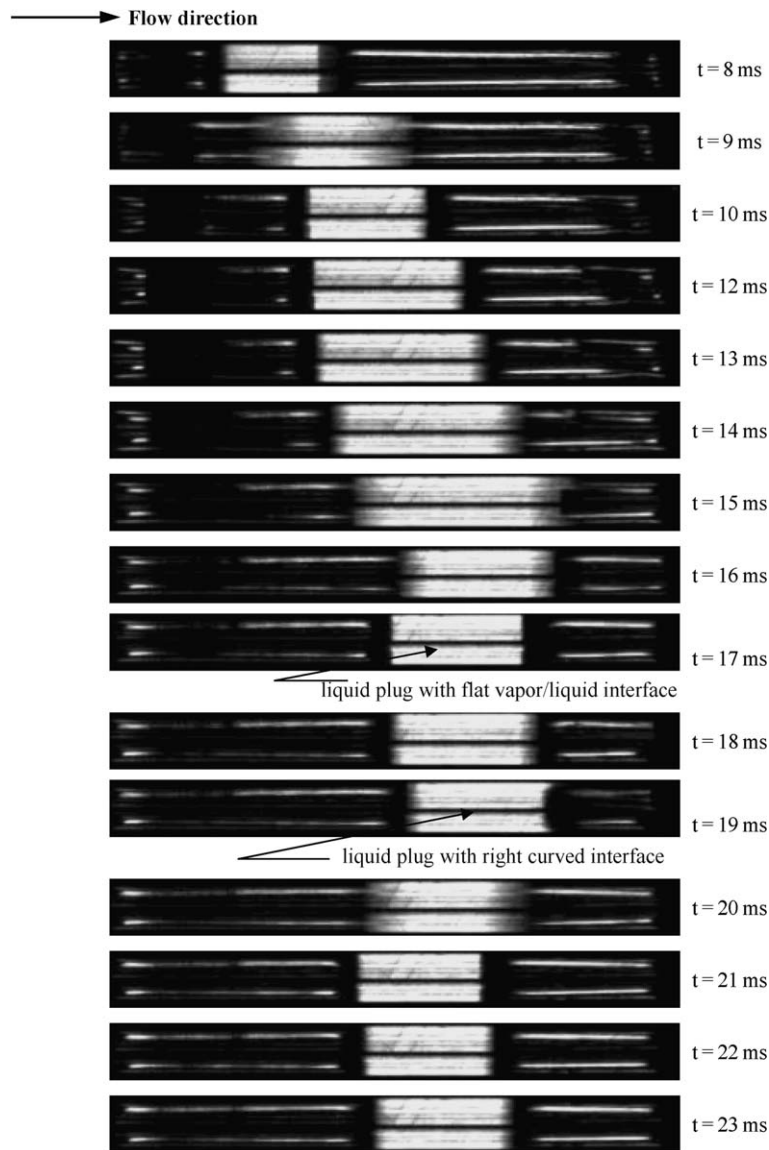

Fig. 10. Liquid plug oscillation in the triangular microchannel ($T_{in} = 28.1$ °C, $T_{out} = 58.4$ °C, $\Delta p = 30.77$ kPa, $G = 46.8$ kg/m^2 s, $q = 90.33$ kW/m^2, microchannel 3 in zone 3).

direction of the liquid plug can be periodically changed between downstream and upstream. The back flow (also named as the flow reversal) can be clearly seen at the time of 19 ms and 20 ms. The curved vapor/liquid interface strongly indicates a positive pressure gradient ($dp/dz > 0$) established at $t = 19$ ms, resulting in the back flow following that time.

3.4.2. Flow pattern B

As commonly recognized previously, stratified flow can happen in macroscale under horizontal or inclined positions (Das et al., 2005). It is governed by the Froude number of the liquid and vapor phases. Besides, as recognized, stratified flow may not encountered in microchannels due to the less effect of the gravity force in confined space. However, we did find such stratified flow by scaling the observed relative positions of the two white lines and the two side corners of the microchannel. The distance between the two white lines is larger than the maximum diameter of a circle that can exist in the cross-section of a triangular microchannel. The only possible arrangement is the half circle indicating the vapor phases with liquids settled down to the bottom of the triangular microchannels (see Fig. 8b, cross-section view of A–A). The two parallel white lines for each microchannel indicate the uniform axial liquid film distributions. Flow pattern B occurs in the early of the transient stratified flow stage and is coming from the collapse of the long liquid plugs.

The present paper concerns the microscale boiling heat transfer at high heat fluxes and low mass fluxes. The corresponding boiling numbers (also named as the dimensionless heat flux) are high. Under such condition, the liquid Froude number cannot be high, but may be in the order of unity, incorporating the hydraulic diameter of 155.4 μm. Thus the gravity force still domains the fluid mechanics thus the stratified flow is possible. In the present data range, the maximum and minimum mass fluxes are 80.56 kg/m² s and 40.74 kg/m² s, corresponding to the liquid Froude numbers (Fr_L) of 7.31 and 1.87.

Hetsroni et al. (2005) observed the annular flow and stated that the liquid film in the cross-section of the triangular microchannel is symmetrically distributed. Besides, Hetsroni et al. (2005) observed the liquid droplets settled down to the bottom of the triangular microchannels during the dry-out stage. Lee et al. (2003) discussed the effects of the microchannel size and shape on the two-phase flow patterns, and stated that annular flow exists in triangular microchannels stably, due to the surface tension force in the three corners of the triangular microchannels. But annular flow may not be stable in the rectangular microchannels.

3.4.3. Flow pattern C and D

Flow pattern B is evolved after the collapse of the long liquid plug in microchannels, but will stay at such state only for a couple of milliseconds. Following then the stratified flow with the axial trapezoid liquid films (flow pattern C and D) is observed (see Fig. 8c, cross-sections A–A and B–B, Fig. 8d, cross-sections of A–A, B–B and C–C). The non-uniform axial liquid film thickness in flow pattern C is resulted from the high boiling numbers, which is defined as $Bo = q/Gh_{fg}$, relating to the K_1 number as proposed by Kandlikar (2004).

$$K_1 = \left(\frac{q}{Gh_{LG}}\right)^2 \frac{\rho_L}{\rho_G} = Bo^2 \frac{\rho_L}{\rho_G} \tag{5}$$

where K_1 consists of the square of the boiling number and the liquid to vapor density ratio. The higher boiling numbers always cause higher K_1 number, leading to the higher momentum force due to the film evaporation at the vapor/liquid interface, which pulls the liquid film of the stratified flow moving toward the downstream of the microchannels, inducing the thicker liquid films accumulated in the downstream of the microchannels. The film evaporation for the stratified flow at high heat fluxes produces a large velocity difference between the escaped vapor and the settled liquid film. Such slip velocity on the interface introduces a force that can be large and is related to the K_1 number as expressed in Eq. (5).

Another mechanism that causes the increased liquid film thickness along the flow direction is the higher vapor shear rate (the velocity gradient perpendicular to the flow direction) adjacent to the liquid film layer, resulting in larger shear stress applied on the settled liquid film. Such shear stress also causes the liquid films traveling from upstream to the downstream and accumulated there. As reviewed by Stone et al. (2004), shear rates $\dot{\gamma}$ can be larger in the microflows. For a simplest case, $\dot{\gamma}$ can be 10^3–10^4 s⁻¹ which are sufficient high to cause non-Newtonian rheological effects if suspended deformable objects are present. The large shear rate in

microchannels are also important to cause the viscous dissipation effect for the single-phase liquid or gas flow (Koo and Kleinstreuer, 2003). Under such condition, the large shear stress takes place on the wall surface. But for the present stratified flow in triangular microchannels, the large shear stress is applied on the settled liquid films.

Flow pattern D is quite similar to flow pattern C, except that there is a steep jumped liquid film thickness near the channel exit for the selected zone, indicating the effect of the transverse trapezoid microchannel.

3.4.4. Flow pattern E

Flow pattern E occurs at the later stage of a full cycle. As shown in Fig. 8e, the top view of the flow patterns indicates four white lines for each triangular microchannel. The cross-section view shows that the four white lines consist of two contact lines for the bottom corner and two contact lines for the two side corners respectively. Actually flow pattern E is a partial dry-out state with liquid films accumulated only in the microchannel three corners. Because flow pattern E is evolved from the flow pattern C or D, the axial liquid film thickness is also non-uniform along the flow direction, that is the film thickness is increased along the flow direction (see cross-section view of A–A and B–B in Fig. 8e).

Lee et al. (2003) also reported the flow pattern E and pointed out that this flow pattern indeed appears to be very stable in the triangular cross-section. The sharp corners of the triangular cross-section suggest the existence of the contact lines. Hydraulic stability requires an intrinsic restoring force to damp out the naturally occurring flow perturbations. Lee et al. (2003) using the simple Young–Laplace equation to explore the existence of the restoring force for the triangular microchannels. The restoring force analysis is also valid for the stable annular flow (but not observed in the present paper) with symmetrical cross-sectional liquid film distributions at higher mass flux than the present paper. Lee et al. (2003) further pointed out that the restoring force
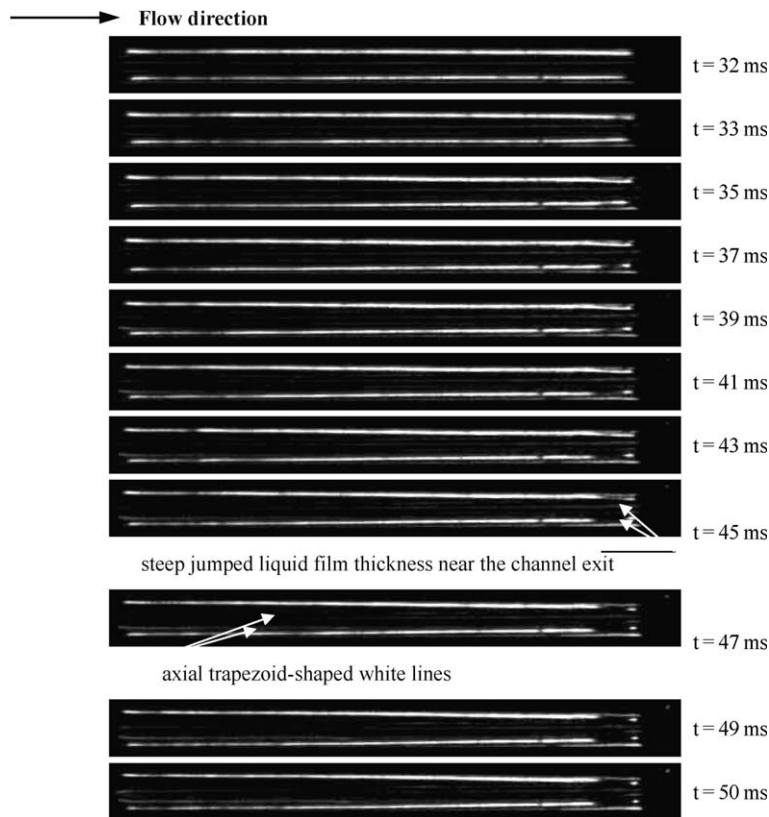

Fig. 11. Successive images showing the transition from flow pattern C to D ($T_{in} = 28.1$ °C, $T_{out} = 58.4$ °C, $\Delta p = 30.77$ kPa, $G = 46.8$ kg/m^2 s, $q = 90.33$ kW/m^2, microchannel 8 in zone 3).

is absent for the rectangular microchannel, that leads to the unstable annular flow in such channel configuration.

3.5. Flow pattern transitions among C, D and E

The top view observed flow patterns for single triangular microchanels are shown in Fig. 11 for the transition from the flow pattern C to D (the flow pattern B can only occur for a couple of milliseconds). The axial trapezoid-shaped liquid films can be identified obviously from the time of 32 ms to 50 ms, indicating the increased liquid film thickness along the streamwise direction, resulted from the higher momentum force and shear stress due to evaporation on the vapor/liquid interface by the higher boiling numbers. The evolution of the steep jumped liquid film thickness near the channel exit gives the strong evidence of the geometry configuration effect. The two side walls of the triangular microchannel in Fig. 11 is immersed by the liquid with the stratified flow.

Fig. 12 shows the transitions from the flow pattern C to E. Four white contact lines (flow pattern E) can be seen from the time of 20 ms, indicating the partial dry-out state with the liquid films accumulated in the three microchannel corners only.

Due to the increased axial liquid film distributions near the three microchannel corners along the flow direction for flow pattern E, the dry-out state occurs earlier in the microchannel upstream. Such transition for a single microchannel can be seen in Fig. 13. The successive images show that the upstream area is fully dry-out but the downstream channel corners are still immersed by the liquid films, following the time of 45 ms in Fig. 13.
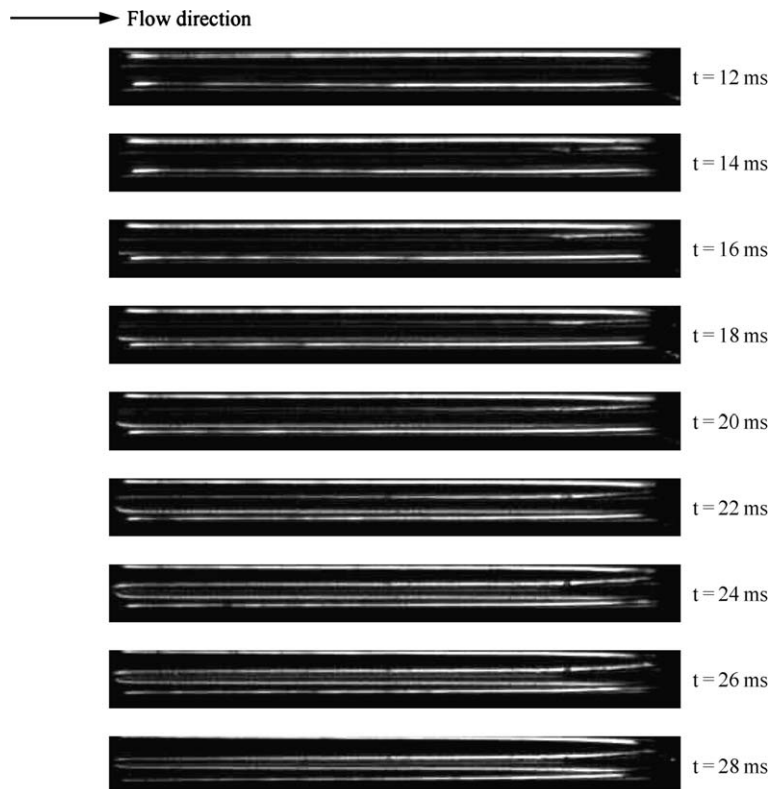

Fig. 12. Successive images showing the transition from flow pattern C to E ($T_{in} = 28.9$ °C, $T_{out} = 56.9$ °C, $\Delta p = 30.32$ kPa, $G = 73.8$ kg/m^2 s, $q = 141.67$ kW/m^2, microchannel 3 in zone 3, four axial trapezoid-shaped white contact lines illustrating the partial dry-out with liquid films accumulated in three channel corners for $t > 22$ ms).
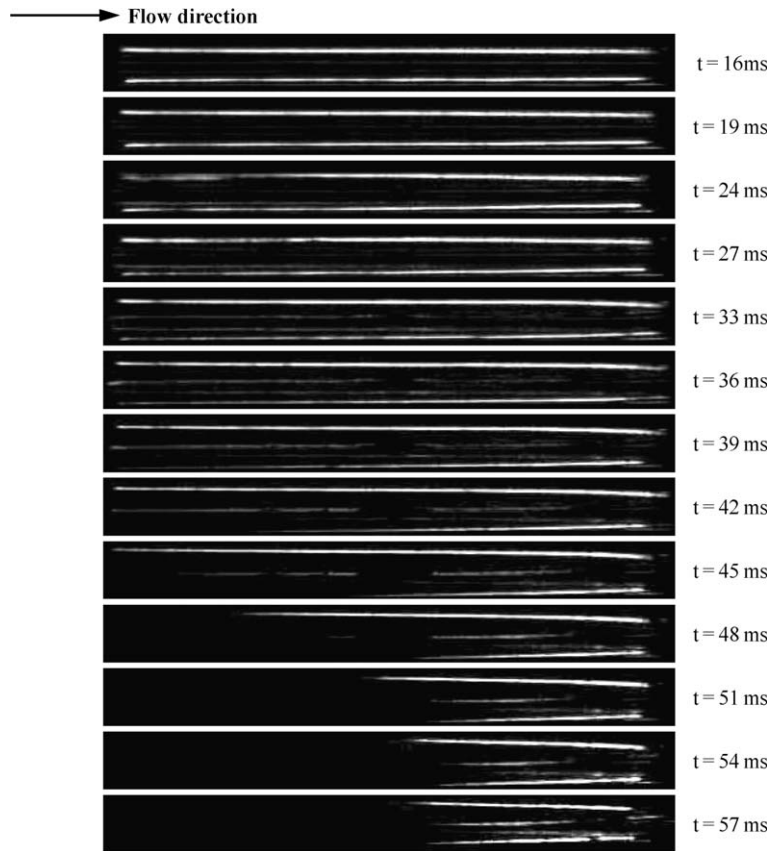
Fig. 13. A set of images showing the transition from flow pattern C to the microchannel upstream dry-out state but liquid films still accumulated in the microchannel downstream corners with increased film thickness along the flow direction ($T_{in} = 33.5$ °C, $T_{out} = 55.8$ °C, $\Delta p = 29.95$ kPa, $G = 58.07$ kg/m^2 s, $q = 106.49$ kW/m^2, microchannel 7 in zone 3).

3.6. Heat transfer behaviors

The silicon chip fabricated using the standard MEMS technique has very small Bi number which is defined as $Bi = h\delta/k$, where h is the heat transfer coefficient between the fluid and the channel wall surface, δ is the effective thickness of the silicon chip, and k is the thermal conductivity of the silicon. For the present study, a rough estimate of the Bi is 0.02 using $h = 10^4$ W/m^2 K, $\delta = 313 \times 10^{-6}$ m and $k = 152$ W/m K, where the effective thickness δ is represented by the distance between the bottom corner of the triangular microchannel and the back surface of the silicon chip. Under such low Bi number, the back surface of the silicon chip can trace the temperature variations of the inside wall surface, which are determined by the heat transfer coefficients between the fluid and the inside wall surface, and the applied heat fluxes. This logic infers that the temperature distributions of the back surface of the silicon chip can follow the dynamic change of the transient flow patterns. Thermal oscillations occur due to the periodic wet and dry-out.

Even though the recording rate of our IR image system is only 4 images per second, which is two orders "slower" than the high speed camera system incorporated with the microscope, the IR image system can still identify the dynamic changes of the back surface temperatures of the silicon chip. A successive of IR images, corresponding to the exact effective heating area of 15.0×4.2 mm^2, are shown in Fig. 14 for the mass flux of 71.03 kg/m^2 s and heat flux of 181.61 kW/m^2. It is seen that the "bright" and "dim" colors occur periodically among two or three successive images, directly indicating the dynamic variations of the back surface temperatures. The relative "bright" colors for some images generally occur at the downstream of the effective heating area, corresponding to the microchannel area of zone 5 (see Fig. 2b).
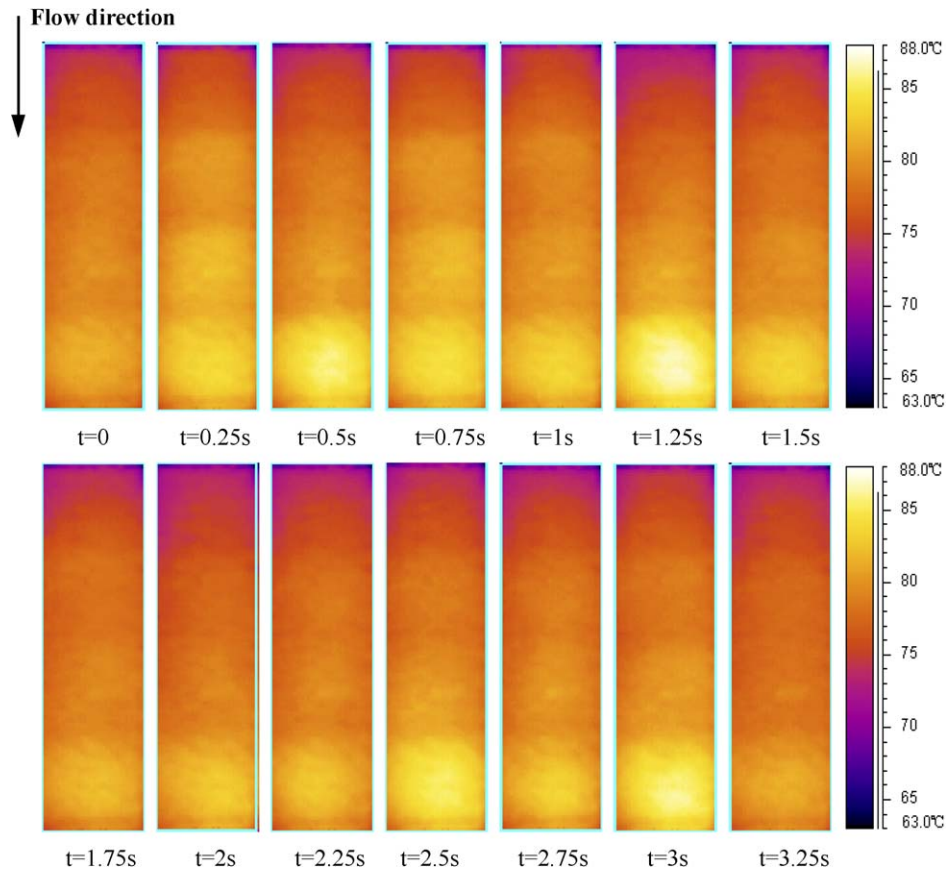
Flow direction

Fig. 14. Color IR image showing the chip temperature field versus time ($T_{in} = 29.8$ °C, $T_{out} = 59.2$ °C, $\Delta p = 31.16$ kPa, $G = 71.03$ kg/m² s, $q = 181.61$ kW/m²).

3.6.1. Temperature distributions of the silicon chip

The three-dimensional chip temperatures relevant to the six successive of temperature measurements are shown in Fig. 15. Such temperature distributions have the following characteristics: (1) The chip temperatures are lower and have a sharp increase at the entrance for a couple of millimeters, corresponding to the single-phase flow length. (2) Following that, the chip temperatures are gradually increased with nearly a constant gradient along the flow direction. (3) The chip temperatures attain the peak distributions in the microchannel area of zone 5. After such peak distribution, they are also sharp decreased in a short distance, due to the solid silicon conduction effect close to the ending of the thin film heater. (4) The chip temperatures are slight higher at the centerline at $y/w = 0.5$, where $w = 4.20$ mm is the width of the heater area. The temperature differences across the whole width direction for any axial locations are less than 2 °C.

3.6.2. Thermal oscillations of the silicon chip

Figs. 14 and 15 show the apparent temperature oscillations, especially at the end of the thin film area relevant to the microchannel area of zone 5. These chip temperature distributions are higher for the time of 2.5 s and 3.0 s. The dynamic heat transfer coefficients are given in Fig. 16 along the streamwise direction at the centerline of $y/w = 0.5$. Indeed the heat transfer coefficients are varied during the period from 2 s to 3.25 s, reflecting the periodic wet and dry-out nature inside the microchannel array of the silicon chip. For any time the heat transfer coefficients have a sharp increase in the single-phase liquid flow area for a couple of millimeters. They are decreased along the flow direction following such short length, indicating the convective heat transfer mechanisms due to the film evaporation on the vapor/liquid interface of the stratified flow. However, a valley
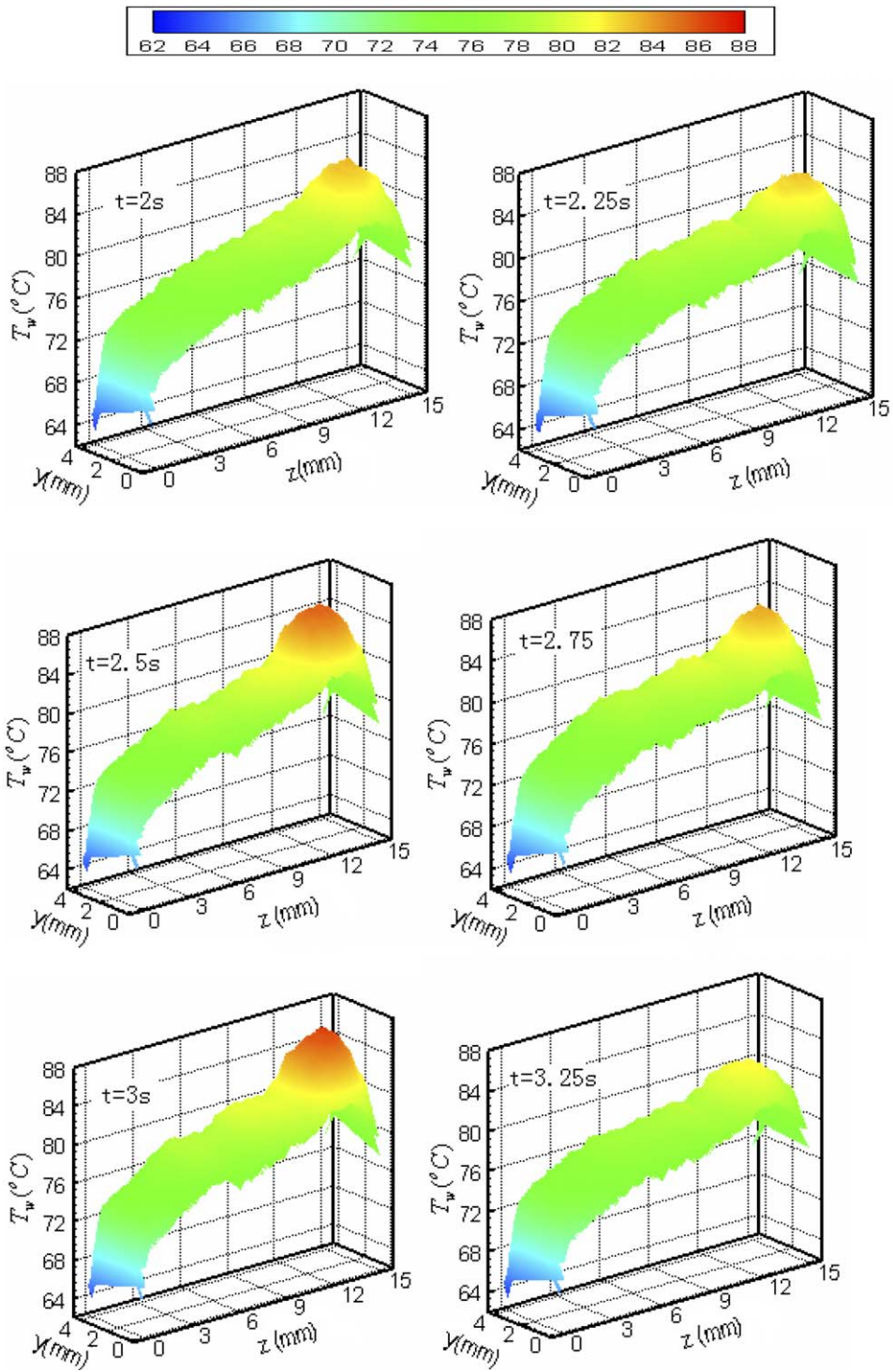
Fig. 15. Three-dimensional chip temperatures versus time for the same run as in Fig. 14.

distribution appears in the end of the thin film area. This is because the higher vapor mass qualities and the higher dry-out possibilities in the ending area of the thin film heater.

For the real application point of view, one may concern the maximum chip temperatures. Because the dry-out possibilities are higher at the ending area of the thin film heater, the maximum chip temperature may take place there and are strongly depended on the heat fluxes. A specific location is selected as ($z = 13.1$ mm, $y = 2.05$ mm), which is in zone 5 at the nearly center of the width direction. In the data range covered, the higher the heat flux is, the higher the chip temperatures. However, the maximum temperatures are less than 88 °C even at the high heat flux of 181.61 kW/m^2 and low mass flux of 71.03 kg/m^2 s for curve 1 in Fig. 17. For all the temperature oscillation curves shown in Fig. 17, the temperature oscillation amplitude seems not to be changed much, with the values between 4 and 6 °C.

3.7. Discussion of the present experimental results

As recognized in the literatures, gravity force has less effect on the flow and heat transfer in microscale. However, the present paper identified the transient stratified flow pattern in intercrossed microchannel arrays. The stratified flow is caused by the low liquid Froude numbers that is coming from the low mass fluxes and
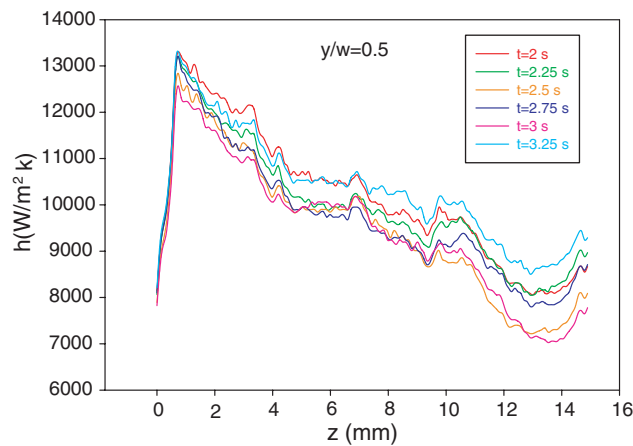

Fig. 16. Heat transfer coefficients along the flow direction at different time ($T_{in} = 29.8$ °C, $T_{out} = 59.2$ °C, $\Delta p = 31.16$ kPa, $G = 71.03$ kg/m^2 s, $q = 181.61$ kW/m^2).
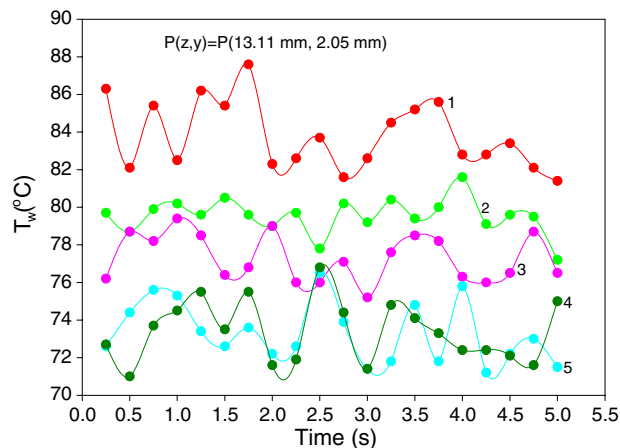

Fig. 17. Chip temperature variations versus time for a specific point for different runs. (1) $T_{in} = 29.8$ °C, $T_{out} = 59.2$ °C, $\Delta p = 31.16$ kPa, $G = 71.03$ kg/m^2 s, $q = 181.61$ kW/m^2. (2) $T_{in} = 28.9$ °C, $T_{out} = 56.9$ °C, $\Delta p = 30.32$ kPa, $G = 73.78$ kg/m^2 s, $q = 141.67$ kW/m^2. (3) $T_{in} = 29.3$ °C, $T_{out} = 59.0$ °C, $\Delta p = 31.84$ kPa, $G = 42.94$ kg/m^2 s, $q = 121.71$ kW/m^2. (4) $T_{in} = 28.1$ °C, $T_{out} = 58.4$ °C, $\Delta p = 30.77$ kPa, $G = 46.80$ kg/m^2 s, $q = 90.33$ kW/m^2. (5) $T_{in} = 33.5$ °C, $T_{out} = 55.8$ °C, $\Delta p = 29.95$ kPa, $G = 58.07$ kg/m^2 s, $q = 106.49$ kW/m^2.

high heat fluxes, and the microchannel array geometry. A lot of factors affect the flow patterns in microchannels. One of them is the effective heating length relative to the whole microchannel length. For the intercrossed microchannel array, any single microchannel array for some separate zones is in the heating area. The initial isolated bubbles occurring near the intercross region of the longitudinal and the transverse microchannels trigger the annular flow at moderate or high mass fluxes and stratified flow at low mass fluxes thus isolated bubbles are not observed in microchannels. In other cases, if the heating length is shorter than that of microchannels, isolated bubbles in microchannels may induce the explosive boiling phenomenon in silicon microchannels(Xu et al., 2005b), which is not observed in the present paper. Therefore the present experimental results can be extended to the normal straight triangular microchannels with the heat flux applied on the whole microchannel length for low mass fluxes and high heat fluxes. Under such conditions, the liquid Froude number is small. Further studies are expected to verify such extension.

4. Conclusions

This paper identifies the transient flow patterns inside the intercrossed microchannel array, displaying the periodic liquid refilling/stratified flow/vapor alternative flow, in the timescale of milliseconds. The fluid pressures and temperatures are found to be stable, and it is explained as that the transient flow evolves so fast that the electronic signals cannot have such fast response.

Even though the surface tension force is important in microscale relative to the gravity force, the gravity force also affects the flow patterns in microscale at the low mass flux. The low liquid Froude numbers showing the same magnitude of the liquid inertia force relative to the gravity force suggests the existence of the stratified flow in microchannels.

Two mechanisms may cause the increased axial liquid film distributions along the flow direction, leading to the earlier dry-out of the microchannel upstream for a separate microchannel zone. However, the dry-out state takes place earlier in the downstream zone than that in the upstream zone.

The transverse trapezoid microchannel strongly affects the flow patterns. Vapor slug may be entrained in the long liquid plug near the triangular microchannel exit. In the stratified flow stage, the steep jumped liquid film is found to exist near the triangular microchannel exit.

The periodic liquid refilling/stratified flow/vapor alternative flow causes the periodic variations of the silicon chip temperatures versus time. Even though the recording rate of the IR image system is two orders slower than the flow pattern observations, the IR image system still identifies the thermal oscillations of the silicon chip surface temperatures.

Acknowledgement

References

Das, G., Das, P.K., Azzopardi, B.J., 2005. The split of stratified gas–liquid flow at a small diameter T-junction. Int. J. Multiphase Flow 31, 514–528.

Ding, Y., Kakac, S., Chen, X.J., 1995. Dynamic instability of boiling two-phase flow in a single horizontal channel. Exp. Thermal and Fluid Sci. 11, 327–342.

Hetsroni, G., Gurevich, M., Mosyak, A., Rozenblit, R., 2003. Surface temperature measurement of a heated capillary tube by means of an infrared technique. Measur. Sci. Technol. 14, 807–814.

Hetsroni, G., Mosyak, A., Pogrebnyak, E., Segal, Z., 2005. Explosive boiling of water in parallel microchannels. Int. J. Multiphase Flow 31, 393–415.

Kandlikar, S.G., 2004. Heat transfer mechanisms during flow boiling in microchannels. ASME J. Heat Transfer 126, 8–16.

Koo, J., Kleinstreuer, C., 2003. Liquid flow in microchannels: experimental observations and computational analysis of microfluidics effects. J. Micromech. Microeng. 13, 568–579.

Lee, M., Wong, Y.Y., Wong, M., Zohar, Y., 2003. Size and shape effects on two-phase flow patterns in microchannel forced convection boiling. J. Micromech. Microeng. 13, 155–164.

Peles, Y.P., Yarian, L.P., Hetsroni, G., 2001. Steady and unsteady flow in a heated capillary. Int. J. Multiphase Flow 27, 577–598.

Stone, H.A., Stroock, A.D., Ajdar, A., 2004. Engineering flows in small devices: microfluidics toward a lab-on-chip. Annu. Rev. Fluid Mech. 36, 381–411.

Wu, H.Y., Cheng, P., 2003a. Liquid/two-phase alternating flow during boiling in microchannels at high heat flux. Int. Commun. Heat Mass Transfer 30, 295–302.

Wu, H.Y., Cheng, P., 2003b. Visualization and measurements of periodic boiling in silicon microchannels. Int. J. Heat Mass Transfer 46, 2603–2614.

Wu, H.Y., Cheng, P., 2004. Boiling instability in parallel silicon microchannels at different heat flux. Int. J. Heat Mass Transfer 47, 3631–3641.

Xu, J.L., Zhou, J.J., Gan, Y.H., Chen, Y., 2004. Unsteady flow phenomenon in a heated microchannel at high heat fluxes. Exp. Heat Transfer 17, 299–319.

Xu, J.L., Zhou, J.J., Gan, Y.H., 2005a. Static and dynamic flow instability of a parallel microchannel heat sink at high heat fluxes. Energy Convers. Manage. 46, 313–334.

Xu, J.L., Gan, Y.H., Zhang, D.C., Li, X.H., 2005b. Microscale boiling heat transfer in a micro-timescale at high heat fluxes. J. Micromech. Microeng. 15, 362–376.

Xu, J.L., Shen, S., Gan, Y.H., Li, Y.X., Zhang, W., Su, Q.C., 2005c. Transient flow pattern based microscale boiling heat transfer mechanisms. J. Micromech. Microeng. 15, 1344–1361.

Xu, J.L., Gan, Y.H., Zhang, D.C., Li, X.H., 2005d. Microscale heat transfer enhancement using thermal boundary layer redeveloping concept. Int. J. Heat Mass Transfer 48, 1662–1674.

Yaws, C.L., 1999. Chemical Properties Handbook. McGraw-Hill, New York.